Center for Turbulence Research
Annual Research Briefs 2009

Full system scramjet simulation

By R. Pečnik, V. E. Terrapon, F. Ham AND G. Iaccarino

1. Motivation and objectives

The development of computational tools that can faithfully reproduce high-Mach number flight conditions is fundamental to improve our ability to realize hypersonic vehicles, especially because physical prototyping is challenging and extremely expensive. Of special consideration in the development of hypersonic vehicles is the accurate evaluation of the safety and operability margins associated with specific design solutions, because of the relatively limited experience with sustained hypersonic flight.

The theoretical performance advantage of scramjets over rockets in hypersonic flight has been well known since the 1950s. For this reason, significant scramjet research has been conducted in many parts of the world. Mainly, three different experimental approaches have been followed to gain experience and physical insight into scramjet propulsion systems: ground testing in continuous flow facilities for Mach<7, high enthalpy shock tunnels with flow durations of the order of 1–10 ms for Mach>7 and more *realistic* ballistic reentry vehicle experiments. A typical example for such a reentry vehicle is the Hyshot flight project devised by the University of Queensland (Smart *et al.* 2006). Postflight data analysis confirmed the presence of supersonic combustion during an approximately 3 s test window at altitudes of 35–29 km. However, due to a radar tracking failure the exact trajectory is not known. To obtain a more comprehensive data set, a ground-based experiment with a 1:1 model for the presumed same conditions as for the flight experiment was conducted by the German Aerospace Center (DLR) in the high enthalpy shock tunnel (Gardner *et al.* 2004). However, to further complement the data, numerical simulations are necessary to gain physical insight in the physics of scramjet engines.

With this objective, we developed a computational infrastructure to solve the Reynolds-averaged Navier-Stokes equations to perform detailed simulations of high-speed vehicles.

The present paper is organized in the following way:

1. Description of the developed Reynolds-averaged Navier-Stokes solver
2. Two-dimensional scramjet simulations to validate the code and to investigate the influence of different equations of state models as well as different turbulence models
3. Application of the code to simulate the full-system 3D scramjet configuration of Hyshot II scramjet.

2. Reynolds-averaged Navier-Stokes solver

A parallel solver for the solution of the compressible Navier-Stokes equations on unstructured meshes has been developed based on a finite volume formulation and implicit time-integration on arbitrary polyhedral meshes. The governing equations are written in conservative form as

$$\frac{\partial}{\partial t}\int_{\Omega}\mathbf{U}d\Omega+\int_{\partial\Omega}\left[\mathbf{F}\left(\mathbf{U}\right)-\mathbf{F}_{v}\left(\mathbf{U}\right)\right]dA=0\ , \tag{2.1}$$

where $\mathbf{U} = \mathbf{U}(\mathbf{x}, t)$ is the state variable, $\mathbf{F}(\mathbf{U})$ and $\mathbf{F}_v(\mathbf{U})$ are the convective and viscous fluxes, respectively, and Ω and $\partial\Omega$ are the physical domain of interest and its boundary.

In particular, we consider

$$\begin{aligned}\mathbf{U} &= [\rho,\ \rho\mathbf{v},\ E]^T \\ \mathbf{F}(\mathbf{U}) &= [\mathbf{n}\cdot\rho\mathbf{v},\ \mathbf{v}\,(\mathbf{n}\cdot\rho\mathbf{v})+p\mathbf{n},\ (E+p)\,(\mathbf{v}\cdot\mathbf{n})]^T \\ \mathbf{F}(\mathbf{U})_v &= [0,\ \mathbf{n}\cdot\Pi,\ \mathbf{v}\cdot(\mathbf{n}\cdot\Pi)+\mathbf{n}\cdot\mathbf{Q}]^T,\end{aligned} \tag{2.2}$$

where ρ, $\mathbf{v}$, p, E, Π, $\mathbf{Q}$, $\mathbf{n}$ represent density, Cartesian velocity vector, pressure, total energy, stress tensor, heat flux vector and outward pointing unit vector normal to the surface, respectively. The discretization scheme is based on a finite volume formulation and implicit time-integration on arbitrary polyhedral mesh elements. The code is entirely written in C++ and uses subdomain decomposition and the message passing interface (MPI) as the parallel infrastructure.

The flow quantities are stored in the cell centers and the governing equations are integrated in conservative form:

$$\frac{\partial\mathbf{U}}{\partial t} = -\mathbf{R}\left(\mathbf{U}\right), \tag{2.3}$$

with

$$\mathbf{R}\left(\mathbf{U}\right) = \frac{1}{V}\sum_f\left[\mathbf{F}\left(\mathbf{U}\right) - \mathbf{F}_v\left(\mathbf{U}\right)\right]A_f\ . \tag{2.4}$$

2.1. *Convective fluxes*

In the past three decades, many different approaches have been introduced to evaluate the convective fluxes; Druguet *et al.* (2005) provides a comprehensive comparison of various methods.

In the present solver we implemented the Roe (1981), the HLLC and the HLLE (Toro 1999) scheme.

The inviscid flux in 1-D can be linearized as

$$\mathbf{F}\left(\mathbf{U}\right) = \mathbf{A}\left(\mathbf{U}\right)\mathbf{U}_x. \tag{2.5}$$

The Jacobian $\mathbf{A}\left(\mathbf{U}\right)$ was replaced by Roe with a constant matrix $\tilde{\mathbf{A}} = \tilde{\mathbf{A}}\left(\mathbf{U}^L, \mathbf{U}^R\right)$, where $\mathbf{U}^L$ and $\mathbf{U}^R$ are the flow states at the two sides of a cell face. This results in a linear system with constant coefficients that retains the initial states of the exact Riemann problem. The derivation of $\tilde{\mathbf{A}}$ is carried out enforcing several constraints: real eigenvalues (hyperbolicity), consistency with the original Jacobian and conservation of fluid properties across the shock; the details are not reported here but can be found in several textbooks, e.g., Toro (1999).

Due to the linearization of the system the resulting discretization is not positively preserving (Einfeldt *et al.* 1991): density and pressure can become negative within the Riemann problem evolution. Although this inconsistency is severe only in near-vacuum conditions, or when strong shocks occur, positivity might also be important in simulations where initial transients may lead to low values of pressure or density.

Furthermore, approximate Riemann solvers obtain all wavespeeds (eigenvalues of the Jacobian matrix) from an arithmetic or a square-root average of the left and right states (as for the Roe scheme). This procedure leads to an underestimation of the expansion-wave velocity, the so-called expansion shock. Another important limitation of these schemes is the so-called carbuncle phenomenon observed, for example, at the stagna-

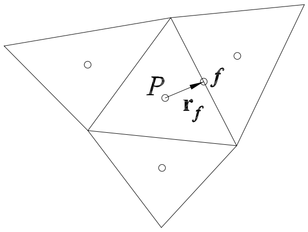

FIGURE 1. Schematic of an unstructured grid with the location of the variables.

tion region of blunt bodies in hypersonic flows. In this region the convective velocity is relatively small compared to the sound speed and errors are *trapped* and deteriorate the solution accuracy (Candler *et al.* 2007; Quirk 1994).

Different solutions have been proposed in the literature and can be separated into two families: eigenvalue limiting methods and hybrid approaches, given in (van Leer *et al.* 1989; Sanders *et al.* 1998; Nompelis *et al.* 2005; Nishikawa & Kitamura 2008).

The approximate Riemann solver used in the present context is the HLLC scheme proposed by Toro *et al.* (1994) and Batten *et al.* (1997). In this method the entropy condition is enforced (no entropy violating discontinuous waves, called rarefaction shocks) and the scheme preserves positivity without the need for additional corrections.

The convective flux is evaluated as

$$\mathbf{F}^{HLLC} = \begin{cases} \mathbf{F}(\mathbf{U}_l) & \text{if } S_L > 0 \\ \mathbf{F}(\mathbf{U}_l) + S_L(\mathbf{U}_l^* - \mathbf{U}_l) & \text{if } S_L \le 0 < S_M \\ \mathbf{F}(\mathbf{U}_r) + S_R(\mathbf{U}_r^* - \mathbf{U}_r) & \text{if } S_M \le 0 \le S_R \\ \mathbf{F}(\mathbf{U}_r) & \text{if } S_R < 0 \end{cases} . \tag{2.6}$$

The wavespeeds S_L and S_R correspond to the left and the right acoustic waves, whereas S_M is related to the intermediate contact/shear characteristic. If the flow is supersonic from left to right, the acoustic wavespeed is $S_L > 0.0$ and the flux has contribution from the left state only; conversely, the flux is evaluated from the right state in the case of $S_R < 0$. In subsonic conditions the flux evaluation is further subdivided to ensure accuracy at the contact surfaces, where U_l^* and U_r^* are the corresponding states. A detailed description of the scheme can be found in Batten *et al.* (1997).

2.2. *Higher-order reconstruction and slope limiting*

The convective flux evaluation illustrated in the previous section leads to a first-order accurate scheme. Second-order accuracy is typically achieved by computing the states at each side of a given cell face using second-order interpolation and then applying the same flux evaluation scheme to the *reconstructed* states. On an unstructured grid the reconstruction is formulated as

$$\phi_f^L = \phi_P + \psi_P \left.\nabla\phi\right|_P \cdot \mathbf{r}_f, \tag{2.7}$$

where $\left.\nabla\phi\right|_P$ is a discrete approximation of the gradient at P, computed using standard least squares approximation or the Gauss theorem, ψ_P is the slope-limiter function and r_f is the vector connecting P and the center of one face as illustrated in Figure 1. Across a discontinuity and, in general, in regions where the solution changes rapidly, the slope-limiter function ψ_P reduces the discrete gradient such that the reconstructed value at the face center maintains monotonicity. In Berger *et al.* (2005) slope limiters are reviewed as well as issues that can arise on unstructured grids.

Two different slope-limiter approaches are implemented in the current flow solver, the solution-dependent weighted least squares method, based on Mandal & Subramanian (2008) and Pečnik *et al.* (2008) and a modified version of the limiter proposed by Barth & Jespersen (1989) and Venkatakrishnan (1995). The second approach is used in the current paper and will be discussed hereafter.

We explored the limiter procedure proposed by Barth & Jespersen (1989) in the framework of unstructured finite-volume schemes. The limiter is computed as follows:

$$\psi_f = \begin{cases} \psi\left(\frac{\delta_+}{\delta_-}\right), & \text{with } \delta_+ = \phi_{\max} - \phi_P \quad \text{if } \phi_f > \phi_P, \\ \psi\left(\frac{\delta_+}{\delta_-}\right), & \text{with } \delta_+ = \phi_{\min} - \phi_P \quad \text{if } \phi_f < \phi_P, \\ 1 & \qquad\qquad\qquad\qquad\quad\; \text{if } \phi_f = \phi_P, \end{cases} \tag{2.8}$$

where $\delta_- = \phi_f - \phi_P$ and $\phi_{\max}$ and $\phi_{\min}$ are the maximum, respectively, and the minimum values of ϕ_P and all neighboring cell centroids. The limiter function is defined as

$$\psi\left(\frac{\delta_+}{\delta_-}\right) = \min\left(1, \frac{\delta_+}{\delta_-}\right). \tag{2.9}$$

The final limiter value ψ_P in Eq. (2.7) is obtained by taking the minimum of all face values ψ_f enclosing the cell centroid P.

Venkatakrishnan (1995) addressed the problem obtaining convergence to steady state using the limiter given in Eq. (2.9). The scheme forms a gradient and limits it by imposing monotonicity conditions in the reconstruction stage across a shock. It is shown that this scheme produces steady-state solutions that are monotone and free of oscillations. However, the residual convergence typically stalls after a few orders of magnitude in particular when nondifferentiable functions such as max or min are used. Therefore Venkatakrishnan (1995) proposed a modification to the limiter in order to achieve residual convergence to machine precision. The min function in Eq. (2.9) has been replaced by a differentiable function

$$\psi\left(\frac{\delta_+}{\delta_-}\right) = \frac{\delta_+^2 + 2\delta_+\delta_- + \varepsilon^2}{\delta_+^2 + \delta_+\delta_- + 2\delta_-^2 + \varepsilon^2}. \tag{2.10}$$

The parameter ε^2 has been introduced to avoid division by zero in regions where $\phi \approx$ constant and is taken to be $\varepsilon^2 = (K\Delta x)^3$, with K a user-specified constant and Δx a characteristic length representing the local mesh size (Venkatakrishnan 1995).

Revisiting Eq. (2.10) and the definition of ε one can see that, in order to achieve unit consistency, the user-specified constant K bears the units from the mesh size and the limiting variable ϕ, which makes this approach less favorable as mesh independency is introduced.

To achieve unit consistency we propose a different definition, with

$$\varepsilon = K\phi_{ref}, \tag{2.11}$$

where ϕ_{ref} represents a strictly positive field of the same units as ϕ, e.g., for limiting the slope of the velocity across a shock we take ϕ_{ref} to be the speed of sound. The constant K defines the amount of ϕ_{ref} to be taken. A value of zero implies that the limiter is active even in near-constant regions, whereas a very high value for K implies no limiting at all. The limiter is expected to ameliorate convergence, however, depending on the

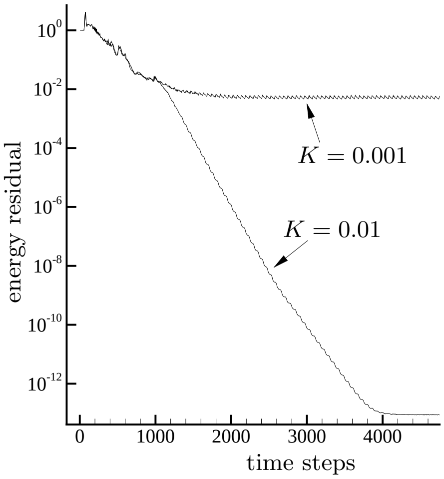

FIGURE 2. Residual of energy for an inviscid Mach 5 cylinder flow.

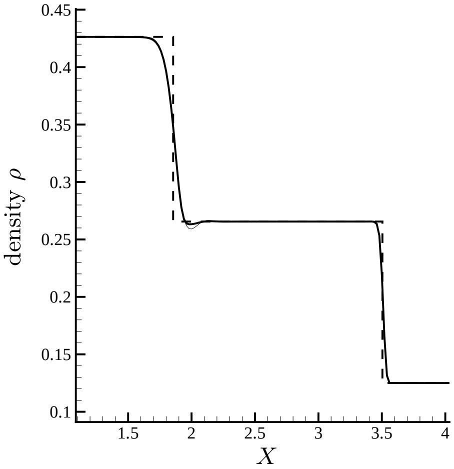

FIGURE 3. Contact discontinuity and shock wave for Sod's shock tube problem; dashed line: exact solution, thick line: $K = 0.001$, thin line: $K = 0.01$.

value of K. Figure 2 illustrates the influence of K on the convergence and monotonicity of the solution. With $K = 0.001$ the convergence stalls after two orders of magnitude, whereas the simulation for the inviscid Mach $= 5$ cylinder with $K = 0.01$ converges to machine precision. On the other hand, a low value of $K = 0.001$ enforces monotonicity, while a higher value leads to a slight under-shoot of density at the contact discontinuity at $X = 2$, (Figure 3). At the shock wave both solutions are monotonic.

2.3. *Viscous fluxes*

The viscous fluxes contain second derivatives of the velocity $\mathbf{u}$ and the enthalpy h. Therefore, gradients at the cell face need to be calculated in an efficient and accurate way. Consider the scalar quantity ϕ, whose gradient at the cell face is $\nabla\phi$. We approximate the normal gradient at the face as

$$\nabla\phi|_f \cdot \mathbf{n}_f = \frac{\phi_{nbr} - \phi_P}{|\mathbf{x}_{nbr} - \mathbf{x}_P|}\alpha_f + \frac{1}{2}\left(\nabla\phi|_P + \nabla\phi|_{nbr}\right) \cdot \left(\mathbf{n}_f - \alpha_f \mathbf{s}_f\right), \tag{2.12}$$

where the subscript f indicates the face with the adjacent control volumes P and its neighbor *nbr* (Ham & Iaccarino 2004). The vector $\mathbf{n}$ is the face normal and $\mathbf{s}$ is the normalized vector connecting the cell centroid across the face f. The gradients $\nabla\phi$ at the cell centers are computed using the Green-Gauss theorem and α is chosen to be the dot product $\alpha = \mathbf{s} \cdot \mathbf{n}$.

2.4. *Implicit pseudo-time integration to steady state*

The discretization of the spatial terms in the Navier-Stokes equations results in a large coupled set of ordinary differential equations of the form given in Eq. (2.3). An implicit scheme is obtained by evaluating the spatial residual terms at the new time level $n + 1$. Since these quantities are not known explicitly, a linearization must be performed about the current time level leading to (Mavriplis 1997):

$$\left(\frac{\mathbf{I}}{\Delta t} + \frac{\partial \mathbf{R}}{\partial \mathbf{U}}\right)\Delta\mathbf{U} = -\mathbf{R}\left(\mathbf{U}^n\right). \tag{2.13}$$

A Taylor expansion is used to formulate the Jacobian matrices for the inviscid and viscous fluxes:

$$\mathbf{F}^{n+1} \approx \mathbf{F}^{n} + \left.\frac{\partial \mathbf{F}}{\partial \mathbf{U}}\right|^{n} \delta\mathbf{U} + O\left(\delta\mathbf{U}\right)^{2} \ . \tag{2.14}$$

The implicit form of the HLLC scheme is based on the decomposition of the wavespeeds reported in Eq. (2.6):

$$\mathbf{F}^{n+1}_{HLLC} = \begin{cases} \mathbf{F}^{n}_{l} + \frac{\partial \mathbf{F}_{l}}{\partial \mathbf{U}_{l}} \delta\mathbf{U}_{l} \\ \mathbf{F}^{n}_{l} + S^{n}_{L}\left(\mathbf{U}^{*n}_{l} - \mathbf{U}^{n}_{l}\right) + \left[\frac{\partial \mathbf{F}_{l}}{\partial \mathbf{U}_{l}} + S^{n}_{L}\left(\frac{\partial \mathbf{U}^{*}_{l}}{\partial \mathbf{U}_{l}} - \mathbf{I}\right)\right] \delta\mathbf{U}_{l} + S^{n}_{L}\frac{\partial \mathbf{U}^{*}_{l}}{\partial \mathbf{U}_{r}} \delta\mathbf{U}_{r} \\ \mathbf{F}^{n}_{r} + S^{n}_{R}\left(\mathbf{U}^{*n}_{r} - \mathbf{U}^{n}_{r}\right) + \left[\frac{\partial \mathbf{F}^{n}_{r}}{\partial \mathbf{U}_{r}} + S^{n}_{R}\left(\frac{\partial \mathbf{U}^{*}_{r}}{\partial \mathbf{U}_{r}} - \mathbf{I}\right)\right] \delta\mathbf{U}_{r} + S^{n}_{R}\frac{\partial \mathbf{U}^{*}_{r}}{\partial \mathbf{U}_{l}} \delta\mathbf{U}_{l} \\ \mathbf{F}^{n}_{r} + \frac{\partial \mathbf{F}_{r}}{\partial \mathbf{U}_{r}} \delta\mathbf{U}_{r} \end{cases} , \tag{2.15}$$

with the Jacobian matrix $\partial\mathbf{F}/\partial\mathbf{U}$ and the matrix $\partial\mathbf{U}^{*}/\partial\mathbf{U}$, which are given in Batten *et al.* (1997).

The viscous flux is linearized as

$$\mathbf{F}^{n+1}_{v} = \mathbf{F}^{n}_{v} + \frac{\partial \mathbf{F}_{v}}{\partial \mathbf{U}_{l}} \delta\mathbf{U}_{l} + \frac{\partial \mathbf{F}_{v}}{\partial \mathbf{U}_{r}} \delta\mathbf{U}_{r} \tag{2.16}$$

with

$$\frac{\partial \mathbf{F}_{v}\left(\mathbf{U}\right)}{\partial \mathbf{U}} = \mathbf{A}_{v} = \frac{\partial \mathbf{F}_{v}\left(\mathbf{Q}\right)}{\partial \mathbf{Q}} \frac{\partial \mathbf{Q}}{\partial \mathbf{U}} \ , \tag{2.17}$$

and with $\mathbf{Q} = \left[u \ v \ w \ T\right]^{T}$ and $\partial\mathbf{Q}/\partial\mathbf{U}$ based on Pulliam & Steger (1982).

The resulting large sparse system (the Jacobian matrices are obtained using first-order discretization) is solved with the generalized minimal residual method (GMRES) using the freely available linear solver package PETSc (Satish *et al.* 2001).

2.5. *Transport scalar solver for the turbulence and combustion model*

The scalar transport equations for the turbulence and combustion models are solved segregated after each *pseudo* time step for the Navier-Stokes equations. In order to solve the scalars in a fast and accurate way, two particular properties need to be ensured:

- consistent inviscid flux evaluations for the scalar and the Navier-Stokes equations; e.g., the mass flux computed with the HLLC approximate Riemann solver is stored and used to compute the scalar advective term and
- no temporal and spatial change for a pure advected scalar, e.g., viscous and source terms are zero, even during the transient phase towards steady state.

The transport equation for a generic scalar ϕ can be written in conservative form as

$$\frac{\partial}{\partial t}\int_{\Omega} \left(\rho\phi\right) d\Omega + \int_{\partial\Omega} \left[\phi\left(\mathbf{n}\cdot\rho\mathbf{v}\right) - F_{v}\left(\phi\right)\right] dA = \int_{\Omega} S\left(\phi\right) \ d\Omega \ , \tag{2.18}$$

where F_v is the viscous flux and $S\left(\phi\right)$ is the scalar source term. The transient term on the left hand side can by expressed as

$$\frac{\partial}{\partial t}\int_{\Omega} \left(\rho\phi\right) d\Omega = \rho \underbrace{\frac{\partial}{\partial t}\int_{\Omega} \phi \ d\Omega}_{\equiv 0} + \phi \frac{\partial}{\partial t}\int_{\Omega} \rho \ d\Omega \ . \tag{2.19}$$

As we are seeking the steady-state solution the term $\frac{\partial}{\partial t}\int_{\Omega} \phi \ d\Omega$ is taken to be zero. Using the conservation of mass from Eq. (2.1) and Eq. (2.2), the second term can be expressed as

$$\frac{\partial}{\partial t}\int_{\Omega}\rho \; d\Omega = -\int_{\partial\Omega}\left(\mathbf{n}\cdot\rho\mathbf{v}\right)\; dA. \tag{2.20}$$

Substituting the continuity equation in Eq. (2.18) we finally get the scalar transport equation for steady-state simulations:

$$\int_{\partial\Omega}\left[\phi\left(\mathbf{n}\cdot\rho\mathbf{v}\right) - F_v\left(\phi\right)\right] dA - \phi\int_{\partial\Omega}\left(\mathbf{n}\cdot\rho\mathbf{v}\right)\; dA = \int_{\Omega} S\left(\phi\right)\; d\Omega\ , \tag{2.21}$$

and in discrete form

$$\sum_f\left[\phi_f m_f - F_{v_f}\left(\phi\right)\right] - \phi_P\sum_f m_f = S\left(\phi\right)\; V\ , \tag{2.22}$$

where m_f corresponds to the mass flux $(\mathbf{n}\cdot\rho\mathbf{v})\, dA$, computed with the HLLC approximate Riemann solver for the mass conservation equation. Once the Navier-Stokes equations reach steady state, the second term on the lefthand side of Eq. (2.22) becomes zero. However, during the transient phase this term is correcting for the non-converged mass conservation while iterating the Navier-Stokes equations. The scalar transport equations are solved implicitly using a biconjugate gradient stabilized method (BCGStab).

2.6. *Implemented turbulence and combustion models*

Currently two different turbulence models are implemented: the one-equation eddy viscosity model of Spalart & Allmaras (1994) and the two-equation turbulence model of Menter (1994). The implemented combustion model is based on the flamelet progress variable approach (FPVA) introduced by Pierce & Moin (2004), and more details of the implementation can be found in Terrapon *et al.* (2009). In the current work only non-reacting simulations are reported, although different models for the gas properties were used, e.g., an ideal gas law and a calorically imperfect gas model using the NASA polynomials to compute the heat capacity at constant pressure c_p and enthalpy h.

3. Hyshot II ground experiment

The ground-based experiment in the High Enthalpy Shock Tunnel (HEG) at the German Aerospace Center (DLR) of a 1:1 model of the HyShot II vehicle (Gardner *et al.* 2004; Karl *et al.* 2008) is investigated in this study. This ground-based experiment provides a more comprehensive data set and better-defined boundary conditions than the original HyShot II scramjet flight experiment. The experiment provides pressure and heat transfer measurements for fuel on conditions along the symmetry line of the wedge intake and the combustor top and bottom wall. Only pressure measurements are reported for the fuel off condition along the combustor walls.

The overall Hyshot II scramjet geometry is given in Figure 4 and 5, where the flow path is from left to right. It consists of a wedge intake and a combustor with constant area terminated by an exhaust nozzle. A bleed channel is located just before the entrance of the combustor to swallow the shock induced by the leading edge of the combustor top wall. Cut A-A shows the combustor top view with the four porthole injectors and the blunt combustor side walls. As no detailed information of the side wall geometry is available at present, we assumed the leading edge to be planar shaped with a thickness of 0.4 mm (the same thickness as the leading edges of top and bottom combustor walls). The free stream inflow conditions are given in Karl *et al.* (2008) and are summarized in Table 1.

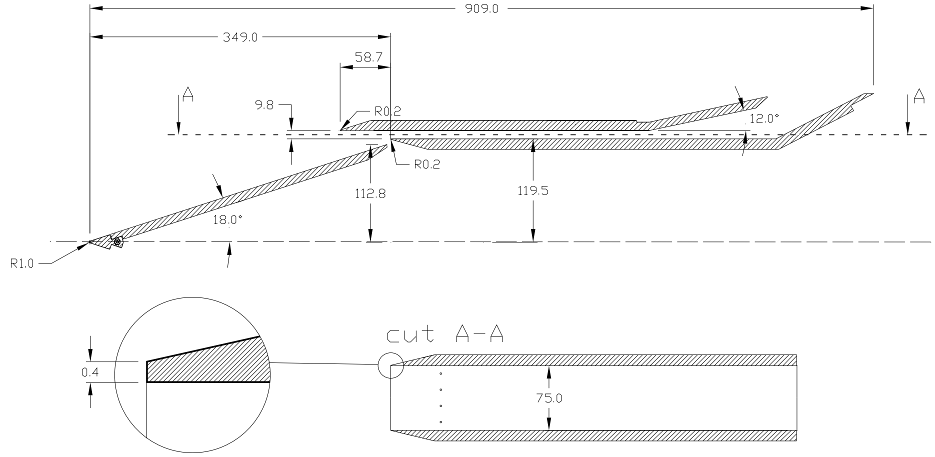

FIGURE 4. Details of the Hyshot II geometry.

Mach number	7.4	
Static pressure	1813	[Pa]
Temperature	242	[K]
Density	0.02596	[kg/m^3]
Flow velocity	2313	[m/s]
Angle of attack	-3.6	[deg]

TABLE 1. Free stream boundary conditions for Hyshot II

4. Results

Figure 5 shows the CFD flow visualization of the full-system scramjet engine Hyshot II simulation. The combustion chamber on top corresponds to fuel off condition, where one can clearly see the diamond-shaped shock structure emanating from the blunt leading edge of the side walls. The bottom combustor corresponds to fuel on condition with the characteristic bow shock structure in front of the hydrogen port hole injectors. More details of the reacting combustor flow simulations are given in Terrapon *et al.* (2009).

4.1. *2D simulations*

In order to reduce computational cost for the investigation of different gas and turbulence models only 2D end-to-end scramjet simulations were performed at first. A mesh independent study was performed with three different resolutions in wall-normal and streamwise directions of the combustor. The simulations reached grid convergence for a grid with 120 cells in wall-normal and 800 cells in streamwise direction for the combustor, which led to a total cell count of 160000 for the 2D end-to-end simulation. The mesh close to the walls was clustered to ensure a y^+ value around unity at the first wall cell, and all 2D results reported hereafter were obtained with this computational grid.

Figure 6 shows a code-to-code validation for the pressure, temperature and velocity combustor inlet profiles. The profiles were extracted at $x = 355$ mm (see Figure 4), shortly downstream of the leading edge of the bottom combustor wall. The discontinuity of the pressure at $y = 0.1235$ clearly indicates the oblique shock caused by this leading

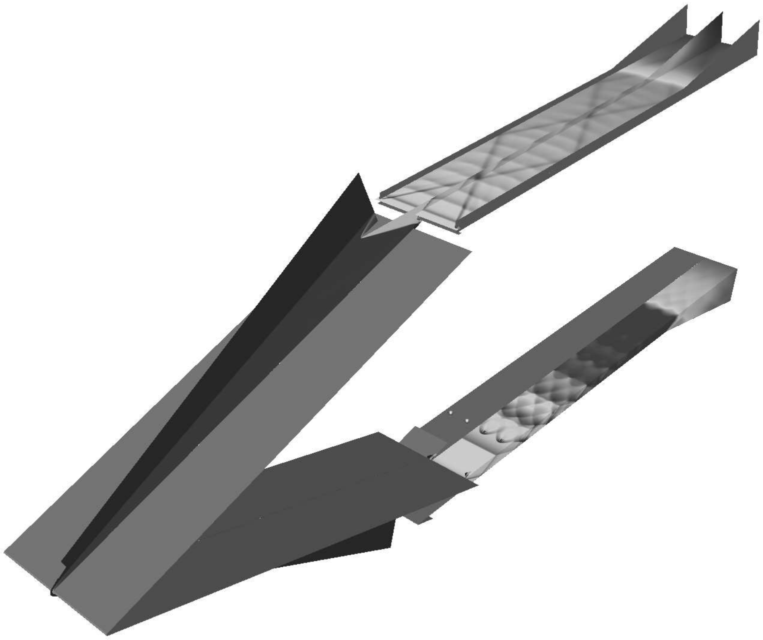

Figure 5. Geometry and CFD flow visualization of the scramjet engine showing the wedge intake (*front*) and combustor with fuel off (*top*) and fuel on conditions (*bottom*), respectively. The contour plots show the square root of pressure.

edge. The influence of different gas models reflects on the shock location and the overall temperature level at the considered location, where the calorically perfect gas gives a higher temperature level and a higher shock angle. The results with the calorically imperfect gas agree well with the DLR Tau simulation reported in Karl *et al.* (2008).

The pressure distribution along the combustor bottom wall is reported in Figure 7. Again two simulations with different gas models were carried out (Figure 7 (*a*)) in order to study their influence on the combustor flow field. Interestingly, the simulation with constant gas properties shows one more reflected shock along the combustor than the DLR experiment and the calorically imperfect gas simulation. This discrepancy can be explained by the difference of the heat capacity ratio γ between these two simulations. The simulation with variable properties gives a value of $\gamma \approx 1.32$ at a temperature of $T = 1300$K inside the combustor, which therefore leads to a higher Mach number with a wider shock train (see also Figure 8). Figure 7 (*b*) shows the results obtained with different turbulence models. There is only a slight difference in the pressure distribution at the end of the combustor, where the Menter SST model agrees better with the experimental values.

4.2. *3D simulations*

The 3D simulation includes the blunt combustor side walls given in Figure 4. In order to decrease the computational domain, only the combustor was modeled, including the leading edges of the bottom and the side wall and symmetry was assumed in the spanwise half plane. The inlet profiles were extracted from the 2D simulation and then interpolated as a Dirichlet boundary condition to the 3D computational domain. Eighty cells were used in spanwise direction, clustered towards the side wall to ensure the same y^+ values

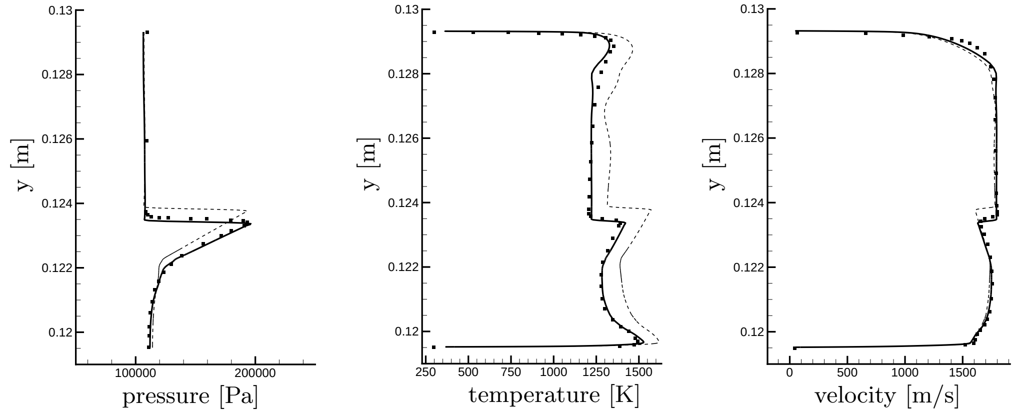

FIGURE 6. Combustor inlet profiles at $x = 355$ mm for pressure, temperature and velocity. Symbols: DLR Tau simulations from Karl *et al.* (2008); dashed line: calorically perfect gas; solid line: calorically imperfect gas; both simulations were performed with the Spalart and Allmaras turbulence model.

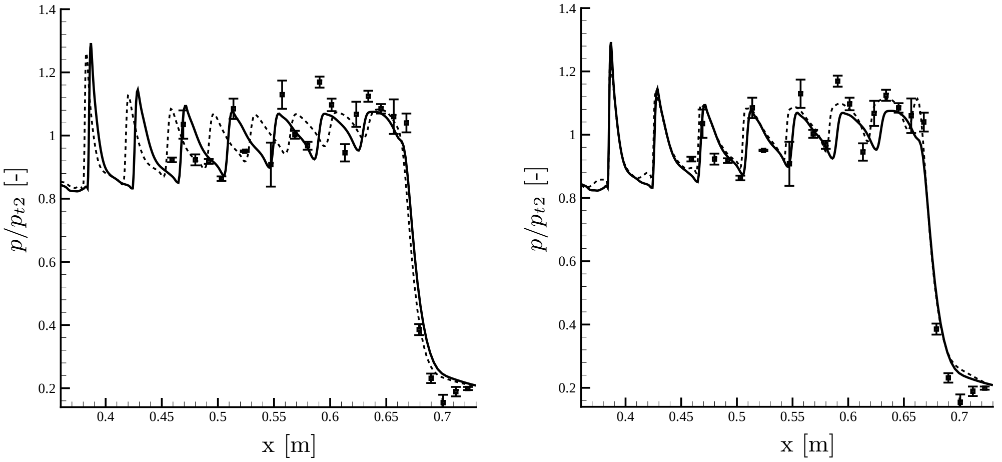

(*a*) Calorically perfect gas (*dashed line*) and calorically imperfect gas (*solid line*), turbulence model: Spalart and Allmaras

(*b*) Menter SST turbulence model (*dashed line*) and Spalart & Allmaras turbulence model (*solid line*), both simulations with calorically imperfect gas model.

FIGURE 7. Normalized pressure distribution along bottom wall for fuel off condition using different models for gas properties and turbulence. Symbols with error bars correspond to the DLR measurements. Pressure is normalized by $p_{t2} = 1.3e5$ taken from Karl *et al.* (2008).

as for the top and bottom walls. The overall computational domain consists of 9M cells. The simulation was performed with the calorically imperfect gas model and the Spalart and Allmaras turbulence model.

Figure 8 shows the velocity divergence for the two channel midplanes to visualize the complex shock structure in the unfueled combustor. Three shock systems with the same shock angle occur: the shock train induced by the leading edge of the bottom wall and two shock trains emanating from the blunt side walls. These shocks intersect at two positions along the center plane and alter the pressure distributions, as can be seen in

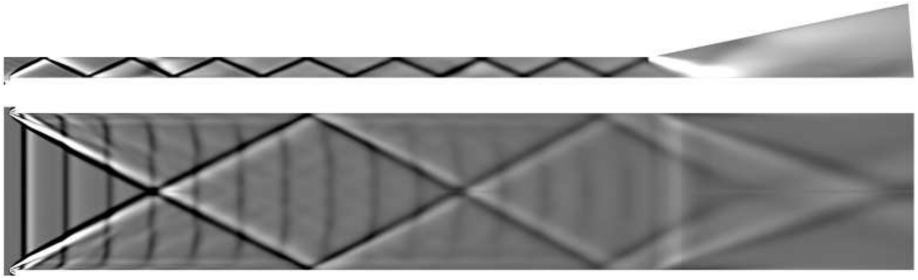

FIGURE 8. Flow visualization at the combustor channel center planes using the velocity divergence.

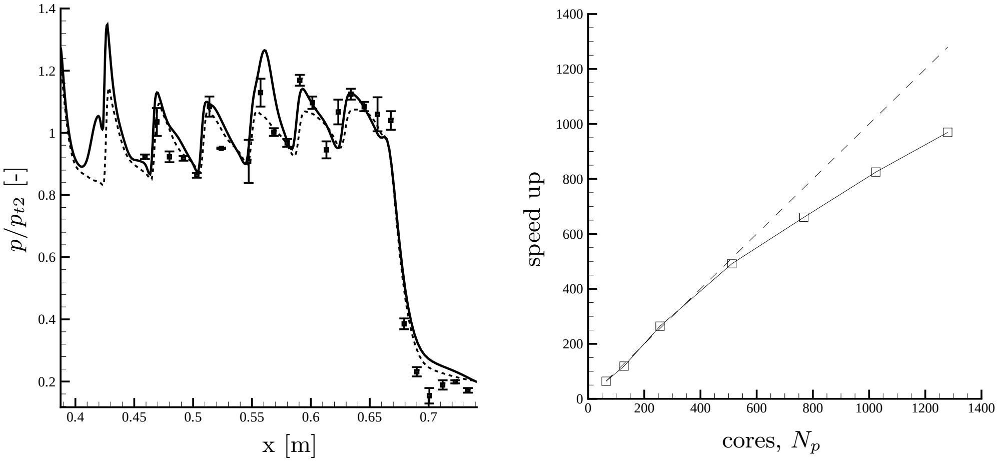

(*a*) Pressure distribution along bottom wall for fuel off condition using different geometrical fidelities. Solid line: 3D with blunt combustor side walls; dashed line: 2D simulation. Symbols with error bars are DLR experiment.

(*b*) Scaling for the for the 3D fuel off combustor; scaling is reported relative to a run with 64 cores.

FIGURE 9. Normalized pressure distribution and code scaling for the 3D scramjet simulation.

Figure 9 (*a*). The agreement between simulation and experiment improves remarkably in the rear part of the combustor as the effect of the side walls is taken into account.

It is important to note that the 3D simulation is a preliminary attempt to investigate 3D effects as the shape of the side wall was not exactly known from the experimental setup. Furthermore, note that the multiple shock intersection at the center plane only occurs for zero yaw angle. A small change in yaw angle would generate a slip surface at the first intersection of the side wall shocks and further complicate the flow field within the combustor.

Figure 9 (*b*) summarizes the code scaling study done at the Lawrence Livermore open computing facility Hera, showing linear scalability up to 600 CPU cores (15000 cells per core) for the present 3D simulation.

5. Conclusion and future work

A fully implicit parallel Reynolds-averaged Navier-Stokes solver based on a finite volume formulation on arbitrary polyhedral mesh elements has been developed during the past two years. Currently, the code contains two different eddy viscosity turbulence models and a combustion model based on the flamelet progress variable approach. The code is entirely written in C++ and uses subdomain decomposition and MPI as the parallel infrastructure.

The code was applied to simulate the Hyshot II scramjet engine to assess the validity of the different models. It was shown that for the high temperature present in a scramjet the use of a calorically imperfect gas model is important and that the turbulence model has only a small impact on the flow solution. To assess the influence of different geometrical fidelities, a 3D simulation of the combustor with side walls was performed, where further improvement of the predictive capability was gained.

The next steps will be to extend the Navier-Stokes solver for unsteady flow simulations and then to perform simulations to investigate the unstart process due to thermal chocking in the combustor of the same scramjet configuration Hyshot II.

Acknowledgements

This work was supported by the US Department of Energy under the Predictive Science Academic Alliance Program (PSAAP) Program.

REFERENCES

Barth T.J., Jespersen, D.C. 1989 The design and application of upwind schemes on unstructured meshes. 27th Aerospace Science Meeting, Reno, NV, AIAA 1989-0366

Batten, P. Leschziner, M. A., & Goldberg, U. C. 1997 Average-state Jacobeans and implicit methods for compressible viscous and turbulent flows. *J. Comput. Physics* **137**, 38-78.

Berger, M., Aftosmis, M. J. & Murman, S. M. 2005 Analysis of slope limiters on irregular grids. 43rd Aerospace Science Meeting, Reno, NV, AIAA 2005-0490.

Candler, G. V., Barnhardt, M. D., Drayna, T. W., Nompelis, I., Peterson, D. M. & S Subbareddy, P. 2007 Unstructured grid approaches for accurate aeroheating simulations. 18th AIAA Computational Fluid Dynamics Conference, Miami, US., AIAA 2007-3959.

Druguet, M. C., Candler, G. V. & Nompelis, I. 2005 Effect of numerics on Navier-Stokes computations of hypersonic double-cone flows. *AIAA Journal.* **43-3**, 616-623.

Einfeldt, B., Munz, C. D, Roe, P. L. & Sjogreen, B. 1991 On Godunov-type methods near low densities. *J. Comput. Physics* **92**, 273.

Gardner, A. D., Hannemann, K., Steelant, J. & Paull, A. 2004 Ground testing of the HyShot supersonic combustion flight experiment in HEG and comparison with flight data. *AIAA Paper 2004-3345*.

Ham, F. & Iaccarino, G. 2004 Energy conservation in collocated discretization schemes on unstructured meshes. *Annual Research Briefs. Stanford, Calif.: Center for Turbulence Research, Stanford*, pp 3-14.

Karl, S., Hannemann, K., Mack, A. & Steelant, J. 2008 CFD analysis of the HyShot II scramjet experiments in the HEG shock tunnel. 15th AIAA International Space Planes and Hypersonic Systems and Technologies Conference, Dayton, Ohio, AIAA 2008-2548.

Mandal, J. C. & Subramanian, J. 2008 On the link between weighted least-squares and limiters used in higher-order reconstructions for finite volume computations of hypersonic equations. *Applied Numerical Mathematics* **58**, 705-725

Mavriplis, D.J. 1997 Unstructured grid techniques. *Annu. Rev. Fluid. Mech.* **29**, 473-514

Menter, F. R. 1994 Two-equation eddy-viscosity turbulence models for engineering applications. *AIAA Journal* **32(8)**, 1598-1605.

Nishikawa, H. & Kitamura, K. 2008 Very simple, carbuncle-free, boundary-layer-resolving, rotated-hybrid Riemann solvers. *J. Comput. Physics* **227**, 2560-2581.

Nompelis, I., Drayna, T. W. & Candler, G. V. 2005 A parallel unstructured implicit solver for hypersonic reacting flow simulation. 17th AIAA Computational Fluid Dynamics Conference, Toronto, Canada., AIAA 2005-4867.

Pečnik, R. , Constantine, P., Ham, F. & Iaccarino, G. 2008 A probabilistic framework for high-speed flow simulations. *Annual Research Briefs. Stanford, Calif.: Center for Turbulence Research, Stanford*, pp 3-17.

Pierce, C.D. & Moin, P. 2004 Progress-variable approach for large-eddy simulation of non-premixed turbulent combustion. *J. Fluid Mech.* **504**, 73-97.

Pulliam, T. H. & Steger, J. L. 1985 Recent improvements in efficiency, accuracy, and convergence for implicit approximate factorization algorithms. 23rd AIAA Aerospace Sciences Meeting. Reno, Nev. 38, AIAA-1985-360.

Quirk, J. J. 1994 A contribution to the great Riemann solver debate. *Int. J. Numer. Methods Fluids* **18**, 555.

Roe, P. L., 1981 Approximate Riemann solvers, parameter vectors, and difference schemes. *J. Comput. Phys.* **43**, 357-372.

Sanders, R., Morano, E. & Druguet, M. C. 1998 Multidimensional dissipation for upwind schemes: stability and applications to gas dynamics. *J. Comput. Physics,* **145**, 511-537.

Satish, B., Buschelman, K., Eijkhout, V., Gropp, W.D., Kaushik, D., Knepley, M.G., McInnes, L.C., Smith, B.F., & Zhang, H. 2009 PETSc Web page, http://www.mcs.anl.gov/petsc.

Smart, M. K., Hass, N. E. & Paull, A. 2006 Flight data analysis of the HyShot 2 scramjet flight experiment. *AIAA Journal* **44**(10), 2366–2375.

Spalart, P. R. & Allmaras, S. R. 1994 A one-equation turbulence model for aerodynamic flows. *Recherche Aerospatiale* **1**, 5-21.

Terrapon, V.E., Pečnik, R. & Pitsch, H. 2009 A flamelet model for supersonic combustion. *Annual Research Briefs. Stanford, Calif.: Center for Turbulence Research, Stanford.*

Toro, E. F. 1999 Riemann solvers and numerical methods for fluid dynamics. A practical introduction. *New York, Springer.*

Toro, E. F., Spruce, M. & Spears, W. 1994 Restoration of the contact surface in the HLL-Riemann solver *Shock Waves* **4**, 25-34.

Van Leer, B., Lee, W. T. & Powell, K. G. 1989 Sonic-point capturing. 9th Computational Fluid Dynamics Conference. Buffalo, NY., *AIAA Paper* 89-1945-CP

Venkatakrishnan, V. 1995 Convergence to steady state solutions of the euler equations on unstructures grids with limiters. *J. Comput. Phys.* **118**, 120-130